

Chiral superconductivity in UTe_2 probed by anisotropic low-energy excitations

Received: 17 February 2023

Accepted: 8 May 2023

Published online: 23 May 2023

 Check for updatesKota Ishihara¹✉, Masaki Roppongi¹, Masayuki Kobayashi¹, Kumpei Imamura¹, Yuta Mizukami^{1,3}, Hironori Sakai², Petr Opletal², Yoshifumi Tokiwa², Yoshinori Haga², Kenichiro Hashimoto¹ & Takasada Shibauchi¹✉

Chiral spin-triplet superconductivity is a topologically nontrivial pairing state with broken time-reversal symmetry, which can host Majorana quasiparticles. The heavy-fermion superconductor UTe_2 exhibits peculiar properties of spin-triplet pairing, and the possible chiral state has been actively discussed. However, the symmetry and nodal structure of its order parameter in the bulk, which determine the Majorana surface states, remains controversial. Here we focus on the number and positions of superconducting gap nodes in the ground state of UTe_2 . Our magnetic penetration depth measurements for three field orientations in three crystals all show the power-law temperature dependence with exponents close to 2, which excludes single-component spin-triplet states. The anisotropy of low-energy quasiparticle excitations indicates multiple point nodes near the k_y - and k_z -axes in momentum space. These results can be consistently explained by a chiral $B_{3u} + iA_u$ non-unitary state, providing fundamentals of the topological properties in UTe_2 .

Since the discovery of superconductivity in the nonmagnetic uranium-based compound UTe_2 , the nature of its superconducting state has been extensively studied^{1–31}. Recent studies have reported several anomalous superconducting properties, including extremely high upper critical field much beyond the Pauli limit^{1–3}, reentrant superconductivity^{3,4}, and little reduction of the Knight shift in the nuclear magnetic resonance (NMR)^{1,5}. These results suggest odd-parity spin-triplet pairing in UTe_2 , as in the case of uranium-based ferromagnetic superconductors³². The symmetry of the superconducting order parameter is closely related to the superconducting gap structure, and the previous studies of low-energy quasiparticle excitations, such as specific heat, thermal transport, and magnetic penetration depth measurements^{6–8}, support the presence of point nodes, consistent with the spin-triplet pairing states.

More intriguingly, recent scanning tunneling microscopy⁹, optical Kerr effect¹⁰, and microwave surface impedance measurements⁶ suggest time-reversal symmetry breaking (TRS) in the superconducting state at ambient pressure. As the sign of imaginary part changes under the time-reversal transformation, the chiral TRSB state requires

multiple order parameter components in complex form. We note that high-pressure studies reveal several superconducting phases^{11–13}, suggesting the presence of multiple order parameters under pressure. Thus, UTe_2 is a prime candidate of a topological chiral spin-triplet superconductor. However, the symmetry of the odd-parity vector order parameter \mathbf{d} , whose magnitude is the gap size and whose direction is perpendicular to the spins of Cooper pairs, is still highly controversial. Especially, the nodal structure of order parameter and whether or not it is chiral in the ground state are important issues to understand the possible topological properties of UTe_2 .

The crystal structure of UTe_2 (Fig. 1a) is classified into the point group D_{2h} , whose irreducible representations (IRs) of odd-parity order parameters are listed in Table 1. In the cases of B_{1u} , B_{2u} , and B_{3u} states, point nodes in the superconducting gap function exist on the k_x , k_y , and k_z -axes (Fig. 1b), respectively, while the A_u state is fully gapped. When the odd-parity order parameter \mathbf{d} is represented by a single IR, the positions of nodes can be detected by the temperature dependence of the change in magnetic penetration depth, $\Delta\lambda(T) \equiv \lambda(T) - \lambda(0)$. This is because the low-temperature superfluid density $\lambda^{-2}(T)$, which is

¹Department of Advanced Materials Science, University of Tokyo, Kashiwa, Chiba 277-8561, Japan. ²Advanced Science Research Center, Japan Atomic Energy Agency, Tokai, Ibaraki 319-1195, Japan. ³Present address: Department of Physics, Graduate School of Science, Tohoku University, 6-3, Aramaki Aza-Aoba, Aoba-ku, Sendai 980-8578, Japan. ✉e-mail: k.ishihara@edu.k.u-tokyo.ac.jp; shibauchi@k.u-tokyo.ac.jp

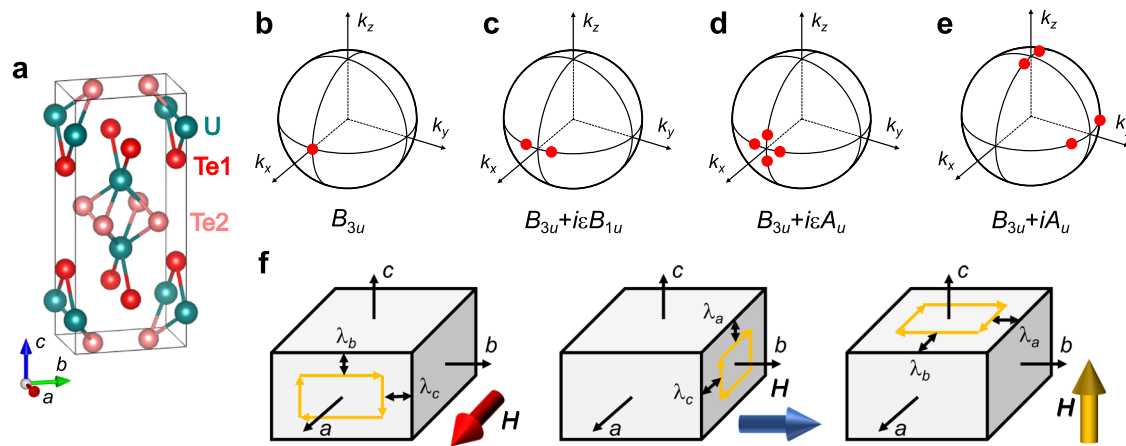


Fig. 1 | Nodal positions of several pairing states in UTe₂ and geometries of anisotropic penetration depth measurements. **a** Crystal structure of UTe₂. Positions of the point nodes (red points) for B_{3u} (**b**), $B_{3u} + i\epsilon B_{1u}$ (**c**), $B_{3u} + i\epsilon A_u$ (**d**), and

$B_{3u} + iA_u$ (**e**) order parameters, where ϵ is a sufficiently small real number. **f** Schematic relations between the directions of the ac magnetic field (big arrows) and λ components.

determined by thermally-excited quasiparticles near the nodes, depends strongly on the directions of the shielding supercurrent density \mathbf{j}_s and the point nodes (whose direction is defined as \mathbf{I}). As a result, when the point nodes are directed along crystallographic α axis ($\mathbf{I}||\alpha$), $\Delta\lambda_\alpha(T)$ follows T^2 dependence, while for perpendicular axes β and γ , $\Delta\lambda_\beta(T)$ and $\Delta\lambda_\gamma(T)$ should follow T^4 dependence (Table 1)³³. Here, the subscript i of λ_i represents the direction of supercurrent density \mathbf{j}_s .

On the other hand, when two symmetries in different IRs accidentally admix to form a TRSB complex order parameter, point nodes are generally located away from the high symmetry axes, and various nodal structures become possible^{10,14}. Considering the $B_{3u} + i\epsilon B_{1u}$ ($B_{3u} + i\epsilon A_u$) state, for example, where ϵ is a sufficiently small real number, a point node of the B_{3u} state splits into two (four) point nodes as depicted in Fig. 1c (Fig. 1d) (for more details, see Supplementary Information I). These split point nodes can be identified as topological Weyl nodes defined by a Chern number^{10,14}, and corresponding Majorana arc surface states are expected³⁴. Although an experimental determination of the exact positions of the nodes is quite challenging in these cases, we can summarize expected nodal positions for different relative sizes of two components in the complex order parameters in Table 2. Thus, by detecting the anisotropy of quasiparticle excitations through direction-dependent physical quantities, such as $\Delta\lambda_i(T)$, we can pin down the superconducting symmetry among the non-chiral and chiral states listed in Tables 1 and 2, respectively.

We use three independent measurements of resonant frequency of the tunnel-diode oscillator (see Methods) with weak ac magnetic field along the a -, b -, and c -axes, in which the shielding current flows perpendicular to the field as described in Fig. 1f. Thus the frequency shift $\Delta f(T)$ consists of two penetration depth components perpendicular to the field direction. As a result, in the single component order parameter cases for point nodes along the α direction, $\Delta f(T)$ for $H_\omega||\alpha$ is the sum of $\Delta\lambda_\beta(T)$ and $\Delta\lambda_\gamma(T)$ components and thus follows T^4 dependence, while $\Delta f(T)$ for $H_\omega \perp \alpha$ should follow T^2 dependence at low T . We

stress that in our measurements the sample is in the Meissner state. Therefore, our approach is an ideal way to investigate the superconducting symmetry in the ground state in the zero-field limit at ambient pressure.

Results

Specific heat

Figure 2a-c show $\Delta f(T)$ in three single crystals of UTe₂ denoted as #A1, #B1, and #C1 respectively (see Supplementary Information V). We observe a large change in $\Delta f(T)$ at 2.1 K (#A1), 1.75 K (#B1), and 1.65 K (#C1) corresponding to the superconducting transition. We note that, while crystals #B1 and #C1 are grown by chemical vapor transport (CVT) method, crystal #A1 is grown by molten salt flux (MSF) method and the transition temperature is the highest value ever reported¹⁵. The clear superconducting transition at $T_c = 2.1$ K, 1.75 K, and 1.65 K for each sample, is also reproduced in the specific heat data (Fig. 2d). Here, we emphasize that a single jump clearly seen in crystals #A1 and #B1 do not necessarily contradict the multi-component order parameter discussed later, because in the Landau theory the jump heights have nontrivial dependence on the coefficients of the fourth power terms of the free energy for chiral superconducting order parameters^{11,35}. However, a recent study¹⁶ has reported that the presence or absence of the double transitions depends strongly on the crystal growth conditions, and the origin of the double transitions is still highly controversial^{17,18}. Figure 2e shows the low-temperature electronic specific heat C_e/T in crystal #A1 as a function of $(T/T_c)^2$. Here, the subtracted phonon contribution is estimated from the previous measurements¹⁹. We can find large quasiparticle excitations following $C_e/T \propto (T/T_c)^2$ down to $0.12T_c$, which is an expected behavior in a

Table 1 | Basis functions, nodal types, and temperature dependence of the magnetic penetration depth for odd-parity order parameters in the point group D_{2h}

IR	Basis functions	Nodes	$\Delta\lambda(T)$
A_u	$k_x\hat{x}, k_y\hat{y}, k_z\hat{z}$	None	$\Delta\lambda_{a,b,c} \propto \exp(- \mathbf{d} /T)$
B_{1u}	$k_y\hat{x}, k_x\hat{y}, k_xk_y, k_z\hat{z}$	Point (k_z)	$\Delta\lambda_{a,b} \propto T^4, \Delta\lambda_c \propto T^2$
B_{2u}	$k_z\hat{x}, k_xk_y, k_z\hat{y}, k_x\hat{z}$	Point (k_y)	$\Delta\lambda_{c,b} \propto T^4, \Delta\lambda_a \propto T^2$
B_{3u}	$k_xk_y, k_z\hat{x}, k_z\hat{y}, k_y\hat{z}$	Point (k_x)	$\Delta\lambda_{b,c} \propto T^4, \Delta\lambda_a \propto T^2$

Table 2 | Expected positions of point nodes in chiral superconducting states with the order parameter $\mathbf{d} = \mathbf{d}_1 + i\mathbf{d}_2$, where \mathbf{d}_1 and \mathbf{d}_2 are classified into different IRs

IR		Positions of point nodes		
\mathbf{d}_1	\mathbf{d}_2	$ \mathbf{d}_1 \ll \mathbf{d}_2 $	$ \mathbf{d}_1 \approx \mathbf{d}_2 $	$ \mathbf{d}_1 \gg \mathbf{d}_2 $
B_{1u}	B_{2u}	near k_y -axis	near k_x -axis	near k_z -axis
B_{2u}	B_{3u}	near k_x -axis	near k_z -axis	near k_y -axis
B_{3u}	B_{1u}	near k_z -axis	near k_y -axis	near k_x -axis
B_{1u}	A_u	None	near k_x - and/or k_y -axes	near k_z -axis
B_{2u}	A_u	None	near k_z - and/or k_x -axes	near k_y -axis
B_{3u}	A_u	None	near k_y - and/or k_z -axes	near k_x -axis

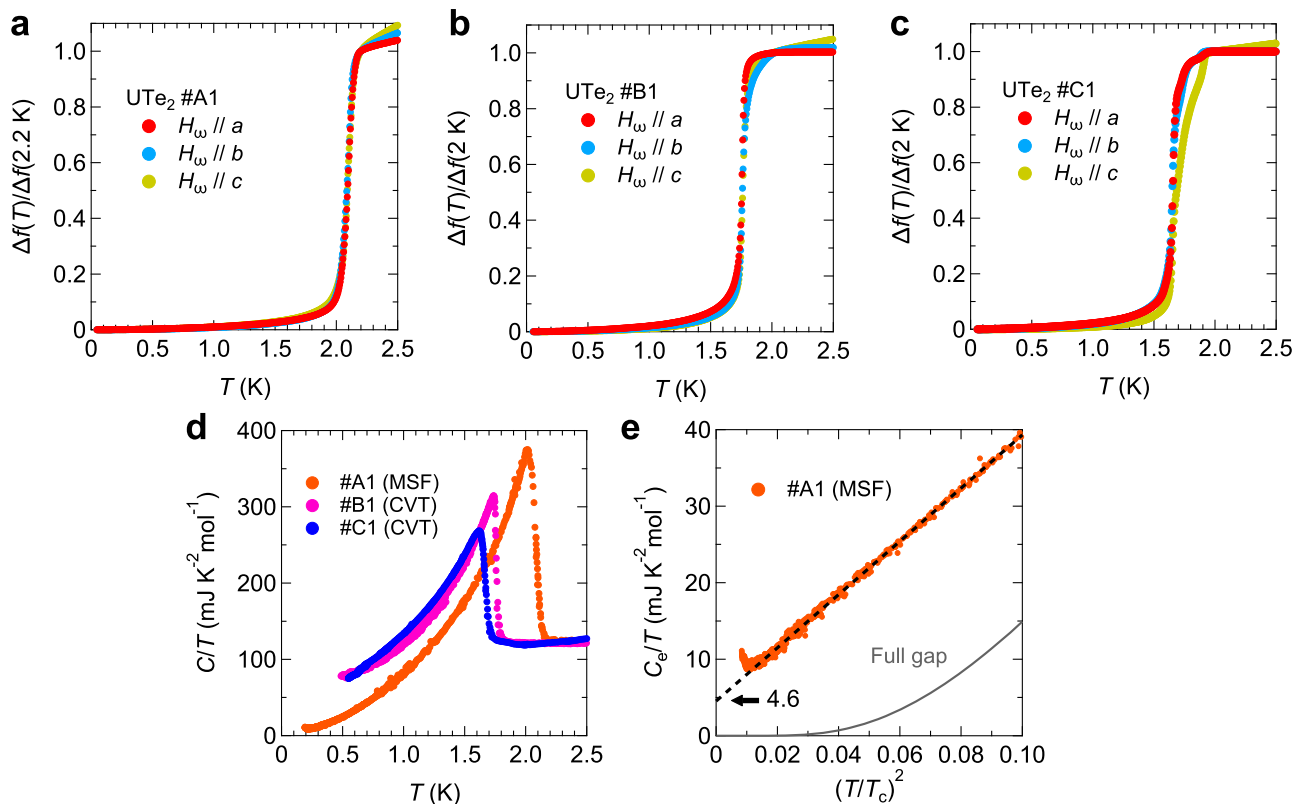


Fig. 2 | Superconducting transitions in UTe₂. **a–c**, Overall temperature dependence of the frequency shift Δf in UTe₂ for crystal #A1 (**a**), #B1 (**b**), and #C1 (**c**). The data of #A1 (#B1 and #C1) are normalized by the value at 2.2 K (2 K). **d**, Temperature dependence of the specific heat C divided by T in crystals #A1, #B1, and #C1 measured at zero field. **e**, Enlarged views of the electronic specific heat C_e/T in crystal

#A1 at low temperatures as a function of $(T/T_c)^2$. The black broken line represents the linear fitting of the data. The gray solid line is the theoretical curve expected for a full gap structure with the gap size $\Delta = 2.2k_B T_c$, which shows a similar size of the specific heat jump with the experiments.

point-nodal superconductor. Furthermore, the residual electronic specific heat γ_0 estimated from the extrapolation of the $C_e/T \propto (T/T_c)^2$ relation is $4.6 \text{ mJ K}^{-2} \text{ mol}^{-1}$, leading to $\gamma_0/\gamma_n = 0.038$, where γ_n is the Sommerfeld coefficient in the normal state. The small γ_0/γ_n value confirms the high quality of crystal #A1. We note that the upturn in C_e/T observed below $0.12T_c$ is caused by the nuclear Schottky contribution¹⁵. While the observed $C_e/T \propto (T/T_c)^2$ behavior and small γ_0/γ_n value indicate the presence of point nodes in the gap structure, we cannot discuss the superconducting symmetry and position of point nodes from the specific heat. Therefore, we rather focus on the low-temperature penetration depth data.

Magnetic penetration depth

The key results are the temperature dependence of $\Delta f(T)$ at low T , which is shown for crystals #A1, #B1, and #C1 in Fig. 3a–c, respectively. The black solid lines represent fitting curves for the data below $0.3T_c$ using the power-law function, $\Delta f(T) \propto T^n$. We note that the exponent values $n = 2.11$ (#A1), 2.07 (#B1), and 1.95 (#C1) for $H_{\omega} \parallel c$ are consistent with the previous ab -plane penetration depth studies^{6,7}. From the fittings, we find that the obtained exponent values for all field directions are nearly equal to 2 or less than 2 in all the samples. This feature can be more clearly seen by plotting $\Delta f(T)$ as a function of $(T/T_c)^2$ as shown in Fig. 3d–f, where all data show almost linear or convex downward curvatures at low T . Thus, our results contradict any cases of single-component odd-parity order parameters, in which $\Delta f(T)$ should follow T^4 dependence when the applied field is directed to the point node direction. Another feature of our data is that the exponent values obtained from $\Delta f(T)$ for $H_{\omega} \parallel a$ and $H_{\omega} \parallel b$ are smaller than that for $H_{\omega} \parallel c$ in crystals #B1 and #C1. Considering that $\Delta f(T)$ consists of two $\Delta \lambda_i(T)$ components perpendicular to the magnetic field (Fig. 1f), our

exponent analysis on these samples indicates that the exponent value of $\Delta \lambda_c(T)$ is smaller than those of $\Delta \lambda_a(T)$ and $\Delta \lambda_b(T)$, which will be discussed in more detail below.

For further investigations of the gap structure, we extract $\Delta \lambda_i(T)$ separately from the $\Delta f(T)$ data for three different field orientations, by considering the geometry of the sample (see Supplementary Information VI). Such an analysis is valid when the magnetic penetration depth is much shorter than the sample dimensions, which holds at low temperatures. To compare the quasiparticle excitations along each crystallographic axis, we discuss the normalized superfluid density $\rho_{s,i}(T) = \lambda_i^2(0)/\lambda_i^2(T)$ and normalized penetration depth $\Delta \lambda_i(T)/\lambda_i(0)$ for three supercurrent directions $i = a, b$, and c , in which evaluations of $\lambda_i(0)$ values are needed. The anisotropy of $\lambda(0)$ can be estimated by the anisotropy of coherence length ξ which can be determined from the initial slope of the temperature dependence of upper critical field $H_{c2}(T)$, when for simplicity we ignore the anisotropy of gap function (see Supplementary Information X). From the $H_{c2}(T)$ data of an ultra-clean sample²⁰, we estimate $\lambda_a(0) : \lambda_b(0) : \lambda_c(0) = \xi_a^{-1}(T_c) : \xi_b^{-1}(T_c) : \xi_c^{-1}(T_c) = 2.01 : 1 : 3.90$. By using the value $\sqrt{\lambda_a(0)\lambda_b(0)} \approx 1 \text{ } \mu\text{m}$ estimated from the previous penetration depth studies^{6,7}, we obtain $\lambda_a(0) = 1420 \text{ nm}$, $\lambda_b(0) = 710 \text{ nm}$, and $\lambda_c(0) = 2750 \text{ nm}$.

The obtained normalized $\Delta \lambda_i(T)/\lambda_i(0)$ as a function of T/T_c for three directions of crystals #A1, #B1, and #C1 are shown in Fig. 4a–c, respectively. First of all, the exponent values n_i obtained from the power-law fitting in $\Delta \lambda_i(T)/\lambda_i(0)$ data are all nearly equal to 2 or less than 2, which is again inconsistent with all the cases of the single component order parameter. Especially, as expected from $\Delta f(T)$ data, $n_c = 1.60$ in crystal #C1 and $n_c = 1.84$ in crystal #B1 are smaller than $n_a \approx n_b \approx 2$. The relatively small n_c in crystals #B1 and #C1 can be more clearly seen by plotting the data as a function of $(T/T_c)^2$ (Fig. 4b,c,

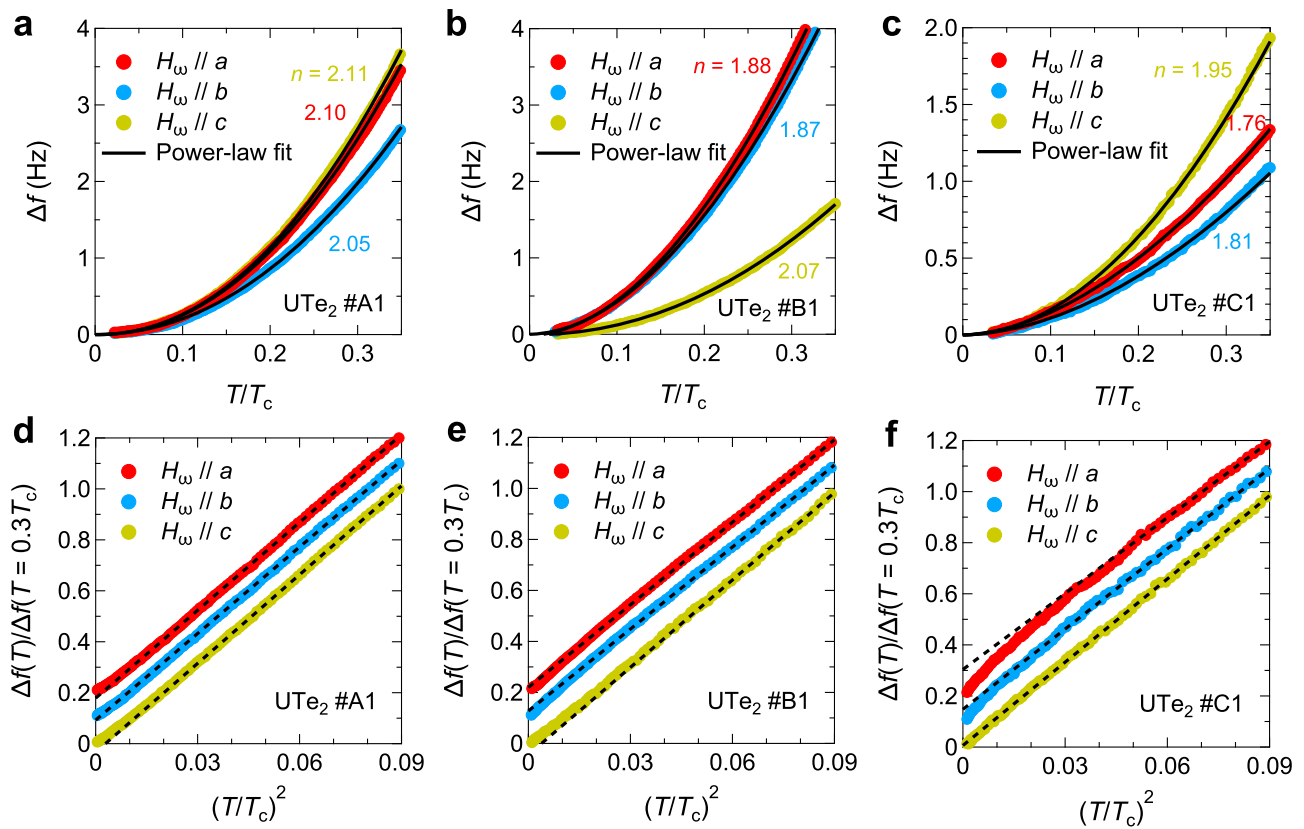


Fig. 3 | Anisotropic frequency shift in UTe_2 for three field directions. Low- T behavior of Δf in UTe_2 for crystal #A1 (a), #B1 (b), and #C1 (c) as a function of T normalized by T_c . Solid lines represent the fitting curves with the power-law function. $\Delta f(T)$ normalized by the value at $T = 0.3T_c$ as a function of $(T/T_c)^2$ in UTe_2 for

crystals #A1 (d), #B1 (e), and #C1 (f). Dashed lines represent T^2 dependence. The data with the field along the a - and b -axes are vertically shifted by 0.2 and 0.1, respectively.

inset). We note that the above discussions are independent from the fitting range of the power-law dependence of $\Delta\lambda(T) \propto T^n$ (see Supplementary Information VII). Another consequence of $\Delta\lambda(T)/\lambda(0)$ results is that the quasiparticle excitations along the b - and c -axes are much larger than those along the a -axis, implying a highly anisotropic nodal structure. Figure 4d-f show the normalized superfluid density, $\rho_{s,i} \equiv \lambda_i^2(T)/\lambda_i^2(0)$, along each crystallographic axis for crystals #A1, #B1, and #C1, respectively, plotted against T/T_c . Compared with theoretical curves for the single order parameter with the supercurrent density \mathbf{j}_s parallel and perpendicular to the direction of point nodes \mathbf{l} , the amount of the excitations along the a -axis is clearly smaller than the $\mathbf{j}_s \parallel \mathbf{l}$ case, while those along the b - and c -axes are as large as the $\mathbf{j}_s \parallel \mathbf{l}$ case.

Discussion

Having established that our anisotropic superfluid density data exclude the single-component odd-parity order parameters, we now discuss the superconducting gap structure based on our experimental results. Adding two order parameters with preserving time-reversal symmetry will not split the point nodes and cannot account for our results (see Supplementary Information II), and thus we need to consider chiral superconducting states formed by two order parameters in different IRs (Table 2). First, we consider chiral superconducting states formed by two B_u IRs. As shown in Supplementary Information I, these chiral states have point nodes located on a symmetric plane of the momentum space. Therefore, small quasiparticle excitations and an exponent value $n_i > 2$ of $\Delta\lambda_i(T)$ are expected for the direction perpendicular to the plane. However, experiments show $n_i \lesssim 2$ for all directions, suggesting that these chiral states are unlikely to be realized in UTe_2 . Thus, we focus on the chiral superconducting states consisting

of the A_u and a B_u IRs. Considering the observed large quasiparticle excitations along the b - and c -axes, we conclude that the $B_{3u} + iA_u$ pairing state is most consistent with our experiments (see Table 2). The reason is that for the $B_{3u} + iA_u$ state with similar sizes of $|\mathbf{d}_{B_{3u}}|$ and $|\mathbf{d}_{A_u}|$ components, multiple point nodes can exist near the k_y - and k_z -axes, leading to larger excitations along the b - and c -axes than along the a -axis. Thus, the quicker decrease of our $\rho_{s,b}$ and $\rho_{s,c}$ data than the $\rho_{s,a}$ data (Fig. 4d-f) is consistent with the $B_{3u} + iA_u$ pairing state. This state can be supported by a recent theoretical study based on the periodic Anderson model, which suggests almost equally stable B_{3u} and A_u states at ambient pressure²¹. We note that the chiral $B_{3u} + iA_u$ state is non-unitary with finite $\mathbf{d} \times \mathbf{d}'$ (see Supplementary Information IV), and for the system close to a ferromagnetic quantum critical point, theory shows that such a non-unitary complex order parameter may become stable²². Moreover, recent studies of NMR Knight shift⁵ suggest finite \hat{y} and \hat{z} components of \mathbf{d} , which is consistent with the $B_{3u} + iA_u$ state. However, we note that the anisotropies of $\lambda_i(0)$ and ξ_i^{-1} are not completely the same in the case of anisotropic superconductors (Supplementary Information X). To confirm the chiral $B_{3u} + iA_u$ state, more direct measurements of $\lambda_i(0)$ are highly desired.

Next we discuss the sample dependence of the small exponent value n_c . We found that the n_c value systematically approach 2 as T_c gets higher (Fig. 4a-c), suggesting that impurity effect is related to the n_c value. In the line node case, the exponent value larger than the clean limit $n = 1$ and smaller than $n = 2$ can be interpreted as a consequence of nonmagnetic impurity scatterings³⁶, quantum criticality³⁷, or non-local effects³⁸. However, these possibilities can be excluded in the case of UTe_2 (see Supplementary Information III). In the presence of point nodes in the gap structure, the impurity scattering can affect only the amplitude of the low-energy excitations, but does not simply change

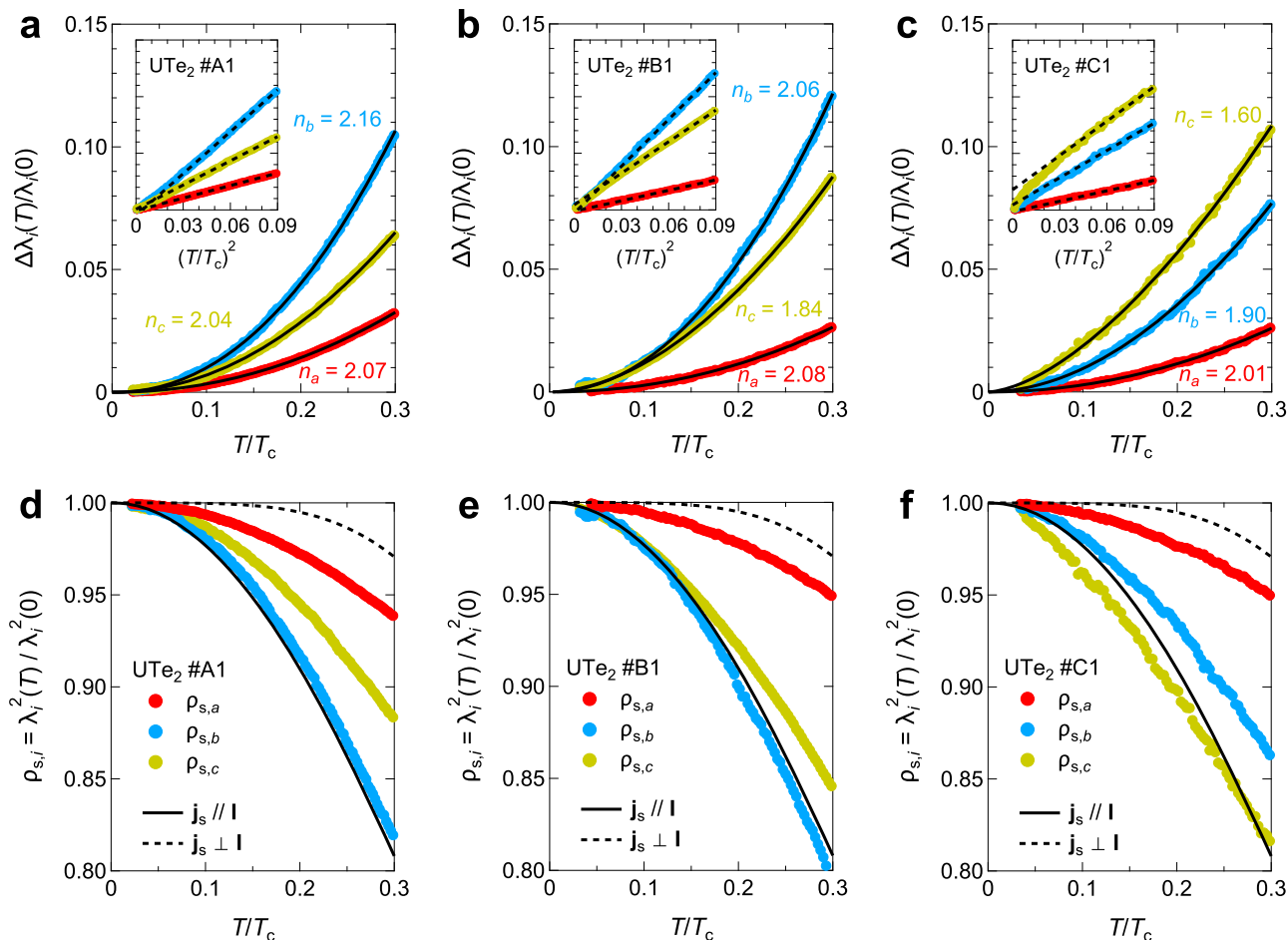


Fig. 4 | Anisotropic penetration depth in UTe_2 for three supercurrent directions. $\Delta\lambda_i(T)$ normalized by $\lambda_i(0)$ for $i = a, b$, and c as a function of T/T_c for crystals #A1 (a), #B1 (b), and #C1 (c). Solid lines in a–c represent the fitting curves of the power-law function and the obtained exponent values are shown in the figures. The inset shows the same data plotted against $(T/T_c)^2$, and the black dashed lines

represent T^2 dependence. Normalized superfluid density calculated from $\Delta\lambda_i(T)/\lambda_i(0)$ data for crystals #A1 (d), #B1 (e), and #C1 (f). Solid and dashed lines represent the theoretical curves for the single order parameter case for j_s parallel and perpendicular to the nodal direction Γ , respectively.

the exponent value of $\Delta\lambda(T) \propto T^2$ ^{6,33}. Here we propose an interference effect of the two point nodes located closely as the origin of the sample-dependent n_c values. In the $B_{3u} + iA_u$ state, the main contributions to $\Delta\lambda_c(T)/\lambda_c(0)$ come from two pairs of two point nodes near the north and south poles along the k_z -axis (Fig. 1e). When the distance of the two nodes near the pole gets sufficiently short, the low-energy excitations can no longer be treated as a sum of the contributions from two independent point nodes, and this interference effect can lead to an exponent value less than 2. We have confirmed that a simple model based on the $B_{3u} + iA_u$ state can indeed lead to an exponent near the experimental n_c value when the two point nodes are sufficiently close to each other (see Supplementary Figs. S12 and S13). Moreover, the observed trend that n_c gets smaller for samples with lower T_c can be consistently explained if we consider that the anisotropic B_{3u} component is more sensitive to impurity scattering than the isotropic A_u component. The reduced B_{3u} component in disordered samples would move the point nodes near the k_z axis closer to each other (Supplementary Information IX), making the interference effect more prominent as observed. We note, however, that the detailed impurity effect on the chiral state requires more microscopic understanding, which deserves further studies.

We should mention that, while recent quantum oscillation measurements revealed quasi-two-dimensional Fermi surfaces (FSs)²³, their precise shape is still under debate. Some theoretical and ARPES studies suggest the presence of a heavy three-dimensional FS around

the Z point, in addition to quasi-two-dimensional FSs mainly formed by Ud orbitals and $Te p$ orbitals^{14,21,24,25}. The presence of the three-dimensional FS is also supported by the relatively isotropic transport properties²⁶. These indicate that there are FSs near k_x -, k_y -, and k_z -axes, which ensures the validity of our discussions on the nodal structure. Also, as for the spin fluctuations in UTe_2 , while NMR and μ SR studies suggest the presence of ferromagnetic fluctuations^{27,28}, recent neutron scattering measurements show only antiferromagnetic fluctuations and no ferromagnetic ones^{29–31}. A possible origin of this discrepancy is the measurement time-scale because the NMR study suggests that the ferromagnetic fluctuations are as slow as the order of kHz, which is too slow to be detected by neutron scatterings. While the magnetic fluctuations are still highly controversial, the ferromagnetic fluctuations may play an important role to induce the $B_{3u} + iA_u$ state, since the magnetic field along a -axis makes a degenerate state of the B_{3u} and A_u state. Thus, our experimental results promote further studies on the pairing mechanism in UTe_2 .

Finally, we note that our conclusion of the $B_{3u} + iA_u$ pairing state is apparently different from the recent report of field angle-resolved specific heat measurements suggesting the point nodes only on the k_x -axis⁸. However, our anisotropic measurements in the Meissner state probe the ground state in the zero-field limit, while the application of strong magnetic field can change the superconducting symmetry^{14,21,22,25}. How the $B_{3u} + iA_u$ state found here changes as a function of field also deserves further investigations.

Summary and perspectives

To sum up, we have found that the frequency shifts of TDO circuit follow T^n dependence with n nearly equal to 2 or less than 2 regardless of sample quality or magnetic field direction. This rules out any of single-component odd-parity states, and thus indicates a multi-component order parameter. The anisotropic penetration depth analysis reveals the presence of multiple point nodes near the k_y - and k_z -axes, which is most consistent with the chiral $B_{3u} + iA_u$ superconducting state in UTe_2 . The presence of TRSB components splits the point node to multiple point nodes away from high-symmetry axes, and in analogy to topological Weyl points in Weyl semimetals, these nodes are expected to create surface arcs of zero-energy Majorana quasiparticles states^{34,39}. Thus UTe_2 is an ideal platform to investigate chiral superconductivity and its related topological physics. In particular, the positions of multiple point nodes (Weyl points) in the bulk studied here are fundamentally important to determine the topological properties of surface states.

Methods

Single crystals of UTe_2 #B1, #C1, and #C2 were grown by the chemical vapor transport method with iodine as the transport agent. Crystal #A1 is grown by the molten salt flux method using a mixture of KCl-NaCl as flux¹⁵ and picked up from the same batch with the crystal showing the RRR about 1000. In both cases, a slightly uranium-rich composition was employed for the starting ratio of U to Te to avoid uranium deficiency¹⁷. The details of the characterizations of the crystals are shown in Supplementary Information V.

To obtain anisotropic components of penetration depth $\Delta\lambda_a(T)$, $\Delta\lambda_b(T)$, and $\Delta\lambda_c(T)$ data separately, we have performed high-precision measurements of ac magnetic susceptibility shift $\Delta\chi(T) \equiv \chi(T) - \chi(0)$ using a tunnel diode oscillator technique operated at 13.8 MHz with weak ac magnetic field H_ω along the three crystallographic axes^{40,41}. The ac magnetic field H_ω induced by the coil of the oscillator is the order of μT , which is much lower than the lower critical field of the order of mT in UTe_2 ²⁰. In this technique, the frequency shift of the oscillator $\Delta f(T) \equiv f(T) - f(0)$ is proportional to $\Delta\chi(T)$.

Specific heat capacity was measured by a long relaxation method in a 3He cryostat or a dilution refrigerator, where a Cernox resistor is used as a thermometer, a heater and a sample stage. The bare chip is suspended from the cold stage in order that it has weak thermal link to the cold stage, and electrical connection for the sensor reading. The samples are mounted on the bare chip using Apiezon N grease. The specific heat of the crystals is obtained by subtracting the heat capacity of bare chip and grease from the total data.

Data availability

The data that support the findings of this study are available within the paper and its Supplementary Information. Source data are provided with this paper.

References

- Ran, S. et al. Nearly ferromagnetic spin-triplet superconductivity. *Science* **365**, 684–687 (2019).
- Aoki, D. et al. Unconventional superconductivity in heavy fermion UTe_2 . *J. Phys. Soc. Jpn.* **88**, 043702 (2019).
- Ran, S. et al. Extreme magnetic field-boosted superconductivity. *Nat. Phys.* **15**, 1250–1254 (2019).
- Knebel, G. et al. Field-reentrant superconductivity close to a metamagnetic transition in the heavy-fermion superconductor UTe_2 . *J. Phys. Soc. Jpn.* **88**, 063707 (2019).
- Nakamine, G. et al. Anisotropic response of spin susceptibility in the superconducting state of UTe_2 probed with ^{125}Te -NMR measurement. *Phys. Rev. B* **103**, L100503 (2021).
- Bae, S. et al. Anomalous normal fluid response in a chiral superconductor UTe_2 . *Nat. Commun.* **12**, 2644 (2021).
- Metz, T. et al. Point-node gap structure of the spin-triplet superconductor UTe_2 . *Phys. Rev. B* **100**, 220504 (2019).
- Kittaka, S. et al. Orientation of point nodes and nonunitary triplet pairing tuned by the easy-axis magnetization in UTe_2 . *Phys. Rev. Res.* **2**, 032014 (2020).
- Jiao, L. et al. Chiral superconductivity in heavy-fermion metal UTe_2 . *Nature* **579**, 523–527 (2020).
- Hayes, I. M. et al. Multicomponent superconducting order parameter in UTe_2 . *Science* **373**, 797–801 (2021).
- Thomas, S. M. et al. Evidence for a pressure-induced antiferromagnetic quantum critical point in intermediate-valence UTe_2 . *Sci. Adv.* **6**, eabc8709 (2020).
- Braithwaite, D. et al. Multiple superconducting phases in a nearly ferromagnetic system. *Commun. Phys.* **2**, 147 (2019).
- Aoki, D. et al. Multiple superconducting phases and unusual enhancement of the upper critical field in UTe_2 . *J. Phys. Soc. Jpn.* **89**, 053705 (2020).
- Shishidou, T., Suh, H. G., Brydon, P. M. R., Weinert, M. & Agterberg, D. F. Topological band and superconductivity in UTe_2 . *Phys. Rev. B* **103**, 104504 (2021).
- Sakai, H. et al. Single crystal growth of superconducting UTe_2 by molten salt flux method. *Phys. Rev. Mater.* **6**, 073401 (2022).
- Rosa, P. F. S. et al. Single thermodynamic transition at 2 K in superconducting UTe_2 single crystals. *Commun. Mater.* **3**, 33 (2022).
- Haga, Y. et al. Effect of uranium deficiency on normal and superconducting properties in unconventional superconductor UTe_2 . *J. Phys.: Condens. Matter* **34**, 175601 (2022).
- Thomas, S. M. et al. Spatially inhomogeneous superconductivity in UTe_2 . *Phys. Rev. B* **104**, 224501 (2021).
- Willa, K. et al. Thermodynamic signatures of short-range magnetic correlations in UTe_2 . *Phys. Rev. B* **104**, 205107 (2021).
- Ishihara, K. Anisotropic enhancement of lower critical field in ultra-clean crystals of spin-triplet superconductor UTe_2 . *Phys. Rev. Res.* **5**, L022002 (2023).
- Ishizuka, J. & Yanase, Y. Periodic anderson model for magnetism and superconductivity in UTe_2 . *Phys. Rev. B* **103**, 094504 (2021).
- Nevidomskyy, A. H. Stability of a nonunitary triplet pairing on the border of magnetism in UTe_2 . arXiv:2001.02699 (2020).
- Aoki, D. et al. First observation of the de Haas-van Alphen effect and fermi surfaces in the unconventional superconductor UTe_2 . *J. Phys. Soc. Jpn.* **91**, 083704 (2022).
- Miao, L. et al. Low energy band structure and symmetries of UTe_2 from angle-resolved photoemission spectroscopy. *Phys. Rev. Lett.* **124**, 076401 (2020).
- Ishizuka, J., Sumita, S., Daido, A. & Yanase, Y. Insulator-metal transition and topological superconductivity in UTe_2 from a first-principles calculation. *Phys. Rev. Lett.* **123**, 217001 (2019).
- Eo, Y. S. et al. c-axis transport in UTe_2 : Evidence of three-dimensional conductivity component. *Phys. Rev. B* **106**, L060505 (2022).
- Tokunaga, Y. et al. ^{125}Te -NMR Study on a Single Crystal of Heavy Fermion Superconductor UTe_2 . *J. Phys. Soc. Jpn.* **88**, 073701 (2019).
- Sundar, S. et al. Coexistence of ferromagnetic fluctuations and superconductivity in the actinide superconductor UTe_2 . *Phys. Rev. B* **100**, 140502 (2019).
- Duan, C. et al. Incommensurate spin fluctuations in the spin-triplet superconductor candidate UTe_2 . *Phys. Rev. Lett.* **125**, 237003 (2020).
- Knafo, W. et al. Low-dimensional antiferromagnetic fluctuations in the heavy-fermion paramagnetic ladder compound UTe_2 . *Phys. Rev. B* **104**, L100409 (2021).
- Duan, C. et al. Resonance from antiferromagnetic spin fluctuations for superconductivity in UTe_2 . *Nature* **600**, 636 (2021).

32. Aoki, D., Ishida, K. & Flouquet, J. Review of U-based ferromagnetic superconductors: Comparison between UGe_2 , URhGe, and UCoGe. *J. Phys. Soc. Jpn.* **88**, 022001 (2019).
33. Groß, F. et al. Anomalous temperature dependence of the magnetic field penetration depth in superconducting UBe_{13} . *Z. Phys. B* **64**, 175–188 (1986).
34. Kozii, V., Venderbos, J. W. F. & Fu, L. Three-dimensional Majorana fermions in chiral superconductors. *Sci. Adv.* **2**, e1601835 (2016).
35. Sigrist, M. & Ueda, K. Phenomenological theory of unconventional superconductivity. *Rev. Mod. Phys.* **63**, 239 (1991).
36. Hirschfeld, P. J. & Goldenfeld, N. Effect of strong scattering on the low-temperature penetration depth of a d-wave superconductor. *Phys. Rev. B* **48**, 4219–4222 (1993).
37. Hashimoto, K. et al. Anomalous superfluid density in quantum critical superconductors. *Proc. Natl Acad. Sci. USA* **110**, 3293–3297 (2013).
38. Kosztin, I. & Leggett, A. J. Nonlocal effects on the magnetic penetration depth in d-wave superconductors. *Phys. Rev. Lett.* **79**, 135–138 (1997).
39. Kallin, C. & Berlinsky, J. Chiral superconductors. *Rep. Prog. Phys.* **79**, 054502 (2016).
40. Prozorov, R. & Giannetta, R. W. Magnetic penetration depth in unconventional superconductors. *Supercond. Sci. Technol.* **19**, R41–R67 (2006).
41. Prozorov, R. Meissner-London state in anisotropic superconductors of cuboidal shape. arXiv:2101.06489 (2021).

Acknowledgements

We thank S. Fujimoto, J. Ishizuka, T. Matsushita and Y. Yanase for fruitful discussions, and N. Abe, and T. Arima, M. Konczykowski, and Y. Tokunaga for technical supports. This work was supported by Grants-in-Aid for Scientific Research (KAKENHI) (Nos. JP22H00105, JP21J10737, JP21H01793, JP21KK0242, JP20H02600, JP19H00649, JP18H05227, JP16KK0106), Grant-in-Aid for Scientific Research on innovative areas “Quantum Liquid Crystals” (No. JP19H05824), Grant-in-Aid for Scientific Research for Transformative Research Areas (A) “Condensed Conjugation” (No. JP20H05869) from Japan Society for the Promotion of Science (JSPS), and CREST (No. JPMJCR19T5) from Japan Science and Technology (JST).

Author contributions

K.H. and T.S. conceived the project. K. Ishihara, M.R., M.K., K.H., and T.S. performed magnetic penetration depth measurements and analyzes the

results. K. Imamura and Y.M. carried out specific heat measurements. H.S., P.O., Y.T., and Y.H. synthesized and characterized single crystals of UTe_2 . K. Ishihara, K.H., and T.S. prepared the manuscript with inputs from Y.H. All authors discussed the experimental results.

Competing interests

The authors declare no competing interests.

Additional information

Supplementary information The online version contains supplementary material available at <https://doi.org/10.1038/s41467-023-38688-y>.

Correspondence and requests for materials should be addressed to Kota Ishihara or Takasada Shibauchi.

Peer review information *Nature Communications* thanks Pierre Rodière, and the other, anonymous, reviewer(s) for their contribution to the peer review of this work. A peer review file is available.

Reprints and permissions information is available at <http://www.nature.com/reprints>

Publisher’s note Springer Nature remains neutral with regard to jurisdictional claims in published maps and institutional affiliations.

Open Access This article is licensed under a Creative Commons Attribution 4.0 International License, which permits use, sharing, adaptation, distribution and reproduction in any medium or format, as long as you give appropriate credit to the original author(s) and the source, provide a link to the Creative Commons license, and indicate if changes were made. The images or other third party material in this article are included in the article’s Creative Commons license, unless indicated otherwise in a credit line to the material. If material is not included in the article’s Creative Commons license and your intended use is not permitted by statutory regulation or exceeds the permitted use, you will need to obtain permission directly from the copyright holder. To view a copy of this license, visit <http://creativecommons.org/licenses/by/4.0/>.

© The Author(s) 2023